Earth Planet. Sci. Lett. 644 (2024) 118924

Contents lists available at ScienceDirect

Earth and Planetary Science Letters

journal homepage: www.elsevier.com/locate/epsl

Pulsed fluid release from subducting slabs caused by a scale-invariant dehydration process

Konstantin Huber *, Timm John *, Johannes C. Vrijmoed, Jan Pleuger, Xin Zhong

Freie Universitaet Berlin, Institut fur Geologische Wissenschaften, Malteserstraße 74-100, Berlin, 12247, Berlin, Germany

ARTICLE INFO

Editor: F.-Z. Teng

Dataset link: https://doi.org/10.5281/zenodo.13226433

Keywords:
Slab dehydration
Chemical heterogeneities
Pulsed fluid production

ABSTRACT

The chemical composition of a rock has a first-order effect on the onset and duration of rock dehydration. We present a multiscale dataset of chemical heterogeneities found in a low-temperature serpentinite from the Mirdita ophiolite in Albania, and we explore the effects of such heterogeneities on slab dehydration during subduction. The dataset consists of chemical and geological mappings from the micron to the meter scale, spanning five orders of magnitude. At each scale, we investigate the interplay of metamorphic reactions as well as porosity and fluid production through thermodynamic modeling along a slab Moho P-T path typical for subducting plates. Notably, our results show that chemical heterogeneities are preserved, regardless of the observation scale, even in the case of local homogenization by events such as the lizardite-antigorite transition. Consequently, scale-invariant patterns of porosity evolution and fluid production along the P-T path emerge, with characteristic peaks for each dehydration reaction. As such, the dehydration behavior on the slab scale seems to be controlled by the processes on the millimeter scale, whereby resulting peaks correspond to pulsed slab fluid release localized in space and time at each scale, along the strike and along the dip of the subducting plate.

1. Introduction

Subduction zones play a crucial role in the Earth's deep water cycle by transporting large amounts of water stored in the hydrated oceanic lithosphere into the mantle (Brovarone et al., 2020; Schmidt and Poli, 1998; Ulmer and Trommsdorff, 1995; Rüpke et al., 2004). The release of this water during slab dehydration, together with the subsequent fluid flow back to the surface, is a process that affects several geological phenomena, including arc volcanism (John et al., 2012; Elliott et al., 1997; Ague et al., 2022), seismicity (Hacker et al., 2003; Ferrand et al., 2017; Shao et al., 2023), and mantle rheology (Hirth and Guillot, 2013; Reynard, 2013; Nakagawa et al., 2015). In addition, slab dehydration mechanisms and subsequent fluid ascent must keep pace with subduction rates on the order of millimeters per year to avoid significant loss of water from the Earth's surface into the mantle (van Keken et al., 2011; Rüpke et al., 2004, 2006; Plümper et al., 2017).

To understand slab dehydration processes, geochemical (Chen et al., 2019; John et al., 2012), geophysical (Bloch et al., 2018), and field-based observations on partially dehydrated exhumed meta-serpentinites show that fluid release from the slab occurs via an interconnected, channeled vein network that forms dynamically during dehydration at depth (Groppo and Compagnoni, 2007; Plümper et al., 2017; Jabaloy-Sanchez et al., 2022; Kempf et al., 2020; Scambelluri et al., 1991). Vein networks associated with mantle dehydration are reported in several localities (Groppo and Compagnoni, 2007; Jabaloy-Sanchez et al., 2022; López Sánchez-Vizcaíno et al., 2009; Scambelluri et al., 1991; Herms et al., 2012; John et al., 2012; Spandler et al., 2011; Ulrich et al., 2024) and often consist of a mineral assemblage rich in metamorphic olivine contrasting with a matrix that often still contains abundant hydrous minerals. The high olivine content within these veins can provide information about the processes controlling their formation and the composition of the percolating fluid.

The formation of such a vein network is thought to occur in three main steps (e.g., Zack and John, 2007; Taetz et al., 2018; Miller et al., 2003). First, at the microscale, fluid is liberated by mineral dehydration. As dehydration progresses, the previously isolated fluid pockets form an interconnected vein network, eventually allowing the fluid to escape from the rock (Taetz et al., 2018). In the first step, dehydration is controlled by the heterogeneities in the local bulk composition (Plümper et al., 2017). In the second step, reactive transport within the porous network becomes important at larger scales (Huber et al., 2022; Chen et al., 2019; John et al., 2012). Finally, fluid escape from the dehydrat-

* Corresponding authors.
E-mail addresses: konstantin.huber@posteo.de (K. Huber), timm.john@fu-berlin.de (T. John).

https://doi.org/10.1016/j.epsl.2024.118924
Received 16 December 2023; Received in revised form 14 July 2024; Accepted 30 July 2024
Available online 19 August 2024

ing rock is likely facilitated by mechanical processes such as hydraulic fracturing (John et al., 2012; Padrón-Navarta et al., 2010) or porosity waves (Connolly and Podladchikov, 2015; Yarushina and Podladchikov, 2015; Yarushina et al., 2022).

The extent to which chemical heterogeneities influence or even control the overall dehydration process as the system evolves from the microscale to larger scales remains uncertain. Huber et al. (2022) demonstrated the importance of centimeter-scale chemical heterogeneities for reactive fluid flow in a dehydrating serpentinite by showing that fluids liberated from silica-poor parts of the rock also have a low silica concentration. These silica-poor fluids can trigger dehydration in other parts of the rock when fluid flow within the porous network is possible. However, the question remains as to what extent such heterogeneities occur at even larger scales and how these variations affect the overall dehydration process.

We present a multiscale dataset from highly hydrated serpentinites of the Mirdita ophiolite in northern Albania. Because the microstructures and composition of our samples fit into the range of other oceanic serpentinites worldwide (e.g., Niu, 2004; Evans and Frost, 2021), we assume the Mirdita serpentinites can be considered as a reasonable case study of serpentinites entering subduction zones worldwide. Spatial variations in silica and iron content occur from the micro-up to the kilometer scale, and we investigate whether the chemical heterogeneity affects dehydration systematics along a typical slab Moho P-T path.

2. Geological setting - the Mirdita ophiolite

Ophiolites of Tethyan origin are common in the Alpine-Himalayan orogenic belt. However, many ophiolites experienced at least a low degree of metamorphism due to tectonic burial, such that their original ocean floor textures and mineral assemblages were modified. Yet, some sections of oceanic lithosphere have undergone only little orogenic metamorphism, like the Mirdita ophiolite of the Western Vardar Zone in northern Albania (Bortolotti et al., 1996; Morishita et al., 2011; Nicolas et al., 1999).

The Jurassic Mirdita ophiolites are situated in the northernmost Hellenides and originate from the Neotethys Ocean, which separated the Adriatic microcontinent from Europe. They formed in a slow-spreading back-arc basin above the subducting Triassic (Meliata) Neotethyan oceanic lithosphere that was part of the Adriatic plate. Following the complete subduction of the Meliata oceanic lithosphere, the ophiolites were obducted onto the Pelagonian zone of the Adriatic margin in the Late Jurassic to Early Cretaceous (e.g., Bortolotti et al., 2005; Schmid et al., 2008; Tremblay et al., 2015). The Western Vardar ophiolites and their Pelagonian sole were imbricated during Alpine orogeny in a piggyback style and formed a stack of nappe complexes, each consisting of ophiolites on top of Adria-derived rocks. The Mirdita ophiolites lie on top of the upper Pelagonian and were not buried under higher tectonic units, thus the temperature gradient in the ophiolite was not significantly raised during Alpine orogeny.

Geochemical and petrological differences further divide the ultramafic massifs of the Mirdita ophiolite into western and eastern units. The signature of the western units indicates a mid-ocean ridge (MOR) origin, in contrast to the predominantly supra-subduction zone (SSZ) signature of the eastern units (Dilek et al., 2007, 2008), with the thickness of the units increasing from 2 to 3 km in the west to 10 to 12 km in the east. We conducted the fieldwork and sampling for this study in the ultramafic Kukes massif in the eastern units of the Mirdita zone, because the eastern units are exposed in a reasonable thickness and comprise all units of the “Penrose style” type of an oceanic lithosphere (Fig. 1). Our hypothesis is that these serpentinites represent a reasonable typical example of a hydrated oceanic lithosphere entering a subduction zone because they contain the right lithological stratigraphy and bulk chemistry as well as characteristic low-temperature mineral assemblages. For a more detailed description of the regional geology, we refer the reader to the Supplementary Information.

3. Methods

3.1. Fieldwork and analytical methods

3.1.1. Sampling

Based on field observations of the ultramafic section of the Mirdita ophiolite, we chose a representative outcrop for detailed lithological mapping (42°01’27”N 20°17’33”E, Fig. 2). The outcrop is located at the eastern portal of the Thirrë-Kalimash tunnel, along a small road built during tunnel construction in 2009, thus providing access to relatively fresh rock. The outcrop is a 16 m long, north-south oriented wall, 3 to 5 m high. Within the outcrop, we identified serpentinized harzburgites and dunites as the primary lithologies and sampled them using a portable drill and rock saw. To prepare the multiscale dataset, we took a representative piece of serpentinized harzburgite and cut from it a circular sample with a diameter of ∼10 cm, sample ALB05. From this sample, we collected six EDS (energy dispersive spectroscopy) maps of varying sizes, from the decimeter scale down to the microscale.

3.1.2. Analytical methods

A ZEISS Axio Imager M2m optical microscope at the Freie Universität Berlin was used to map entire thin sections using reflected and plane polarized transmitted light. Subsequently, selected regions on the thin sections were mapped in the ZEISS Automated Mineralogy Lab at the Freie Universität Berlin using a ZEISS Sigma 300 VP field-emission scanning electron microscope, integrating two energy dispersive X-ray silicon drift detectors (Bruker Quantax XFlash 6, 60 mm^2). The measurements were performed with an acceleration voltage of 20 kV, an aperture size of 120 µm, and a dwell time of 100 ms. To obtain the multiscale dataset, we collected six maps on a representative region by varying the size of the domain and the pixel resolutions: 76, 36, 20, 10, 5, and 2.5 µm, respectively. Quantitative wavelength dispersive spectroscopy (WDS) point analyses on the harzburgite (sample ALB09-1) and dunite (sample ALB06-1) were carried out using the JEOL JXA 8200 Superprobe at Freie Universität Berlin, using an acceleration potential of 20 kV, a beam current of 20 nA, and a beam size of 1 µm. Table 1 shows a summary of representative analyses. Raman mapping was performed to reveal characteristics of the serpentinite and brucite mineral phase distribution within a domain of 40 × 60 µm on a typical mesh texture of the dunite sample ALB06-2. We used a WiTec alpha 300 R spectrometer at Freie Universität Berlin equipped with a Zeiss EC Epiplan 50X/0.75 objective and a polarized solid-state laser with a wavelength of 532.1 nm. Because brucite grains are sensitive to the laser heating, potentially triggering a dehydration reaction, we set the laser power to ∼1 mW, using a pixel dwell time of ∼10 s and step size of 0.5 µm. The obtained Raman spectra were fitted with a MATLAB script to obtain the peak position and peak area. The peaks at 230 cm and 1100 cm were taken to identify the distribution of lizardite and chrysotile (Compagnoni et al., 2021; Groppo et al., 2006), whereas the peak at 440 cm was used to characterize brucite (Groppo and Compagnoni, 2007).

3.2. Upscaling method

For upscaling, we selected representative areas of 1 × 1 mm for the millimeter scale on the 2.5-µm pixel size map, 1 × 1 cm for the centimeter scale on the 20-µm pixel size map, and 5 × 5 cm for the decimeter scale on the 76-µm pixel size map. We considered an area representative if it contained the prominent textural and chemical heterogeneities found at that scale (Fig. 2). From the millimeter to the decimeter scale, this includes the difference between bastites and mesh texture; from the meter to outcrop scale, this includes the lithological difference between dunites, harzburgites, and pyroxenites.

To create the meter-scale dataset, we rearranged and resized the geological map (Fig. 2C). We saved an image of the rearranged outcrop at a resolution of 100 × 100 pixels so that each pixel represented 1 dm^2.

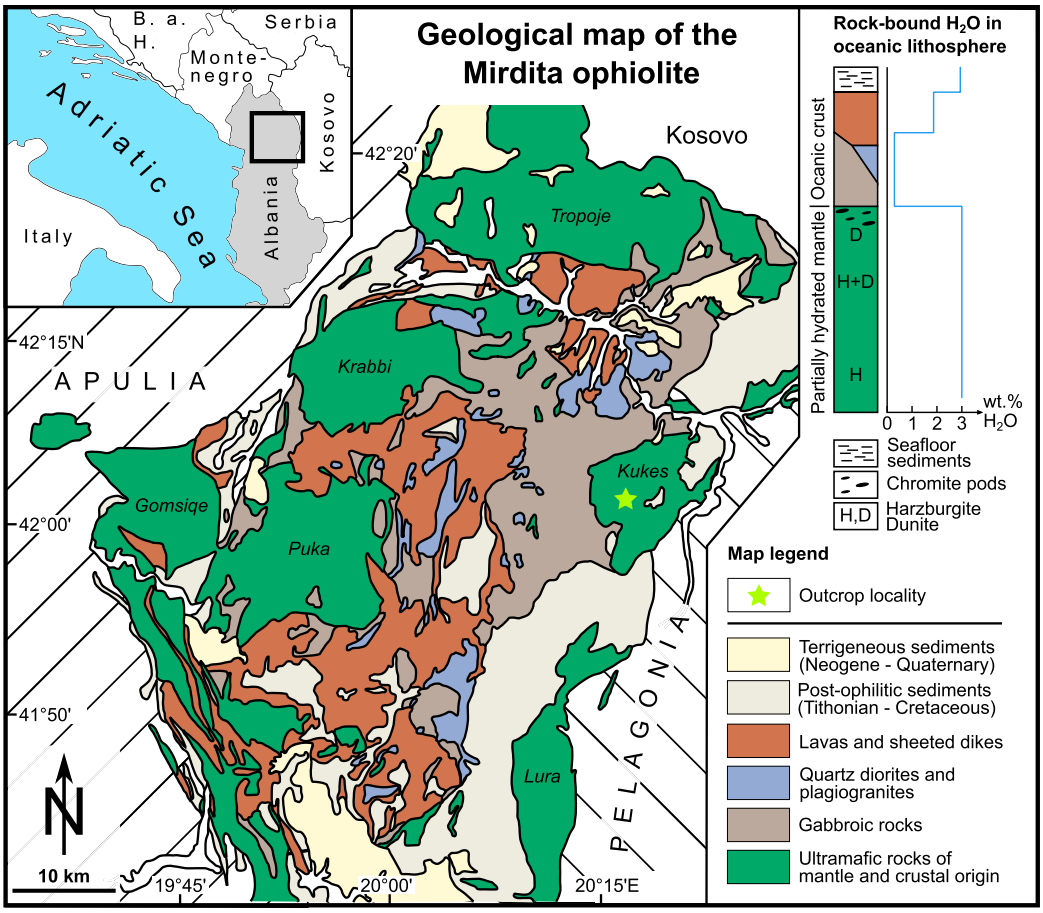

Fig. 1. Geological map of the Mirdita ophiolite in northern Albania [redrawn from Bortolotti et al. (2005)] with green areas marking the occurrence of ultramafic units. The yellow star in the Kukes massif highlights the outcrop's location. The top right panel shows a simplified lithostratigraphic chart representative of the eastern part of the Mirdita ophiolite. Dunite content and the abundance of chromite pods in the ultramafic section increase with proximity to the Moho. Note that the sketch of the rock column is not to scale. The graph to the right of the column shows estimates of H2O bound in the solid for the different lithologies [from Rüpke et al. (2004)]. The 3 wt.% bulk H2O in the mantle implies about 20% hydration of the upper mantle, which contains up to 13 wt.% when fully serpentinized.

We then assigned each pixel a bulk composition based on the lithology that each pixel represented on the geological map. As harzburgite bulk composition, we used 46 wt.% SiO_2, 42 wt.% MgO, and 9 wt.% FeO; as dunite bulk composition, we used 41 wt.% SiO_2, 44 wt.% MgO, and 10 wt.% FeO; for the pyroxenite bulk composition, we used 56 wt.% SiO_2, 35 wt.% MgO and 5 wt.% FeO. To add bulk composition variations within each lithology, we varied each composition by using a Gaussian distribution with the bulk composition as the mean value and a standard deviation of 4 wt.% for both SiO_2 and MgO and 3 wt.% for FeO. The chemical heterogeneities and thus the bulk composition variations produced by this method are within the natural range found in oceanic peridotites and dunites (Niu, 2004) and reflect observations in partially serpentinized high-pressure units such as Erro Tobbio (see, e.g., Peters et al., 2020).

For the final dataset, we performed the map coarsening for each of the selected representative areas (mm, cm, and dm scales) and the rearranged outcrop (m scale) by dividing the chemical maps of the respective domains into a coarser grid of 10×10 pixels (Fig. 2C) and applying a volumetric averaging (e.g., Zhang et al., 2021) within each of these coarse pixels. We considered the area covered by the coarse pixel as the effective thermodynamic domain size, i.e., an area over which the domain behaves as a chemically effective bulk volume for which we explore the mineral assemblage, porosity formation, and fluid production by applying equilibrium thermodynamics. Our approach led to thermodynamic equilibrium domain sizes of 0.01 mm^2 for the millimeter scale, 1 mm^2 for the centimeter scale, 2.5 cm^2 for the decimeter scale, and 1 m^2 for the meter scale. A similar approach of varying thermodynamic domain sizes was used by Plümper et al. (2017), who additionally used a diffusion model to obtain a local bulk composition. For the sake of simplicity, we apply this rather simplified concept. We refer to Evans et al. (2013) for a detailed discussion about exploring length scales of equilibrium for mineral reactions and system and domain sizes of equilibrium in the context of serpentinization/deserpentinization.

3.3. Thermodynamic model and porosity calculation

3.3.1. Phase equilibria calculations

To study the effect of the chemical variations found in the chemical mappings at each scale (mm, cm, dm, and m scale; Fig. 2C), we performed Gibbs free energy minimization calculations along a typical slab Moho P-T path in a subduction zone (Fig. 6A) for every composition (pixel) in the coarse 10×10 pixel maps of each scale. For the thermodynamic calculations, we used Thermolab codes (Vrijmoed and Podladchikov, 2022) with the thermodynamic dataset tc-ds633 from Holland and Powell (2011). Calculations were done in the FMSH (FeO-MgO-SiO_2-H_2O) chemical subsystem, with values for SiO_2, FeO, and MgO taken from the coarse chemical maps (e.g., those of the mm scale in Fig. 5) and H_2O in excess. Additional calculations were done considering Al_2O_3 (FMASH) and with variations of the Fe^{3+}/Fe_{ToT} (FMSHO). The solid phases considered in our calculations were lizardite, antigorite, brucite, talc, orthopyroxene, and olivine. For chemically more complex calculations (FMASH and FMSHO), magnetite and chlorite were also considered. We accounted for the effects of Fe-Mg partitioning for each solid phase using the solution models of Evans and

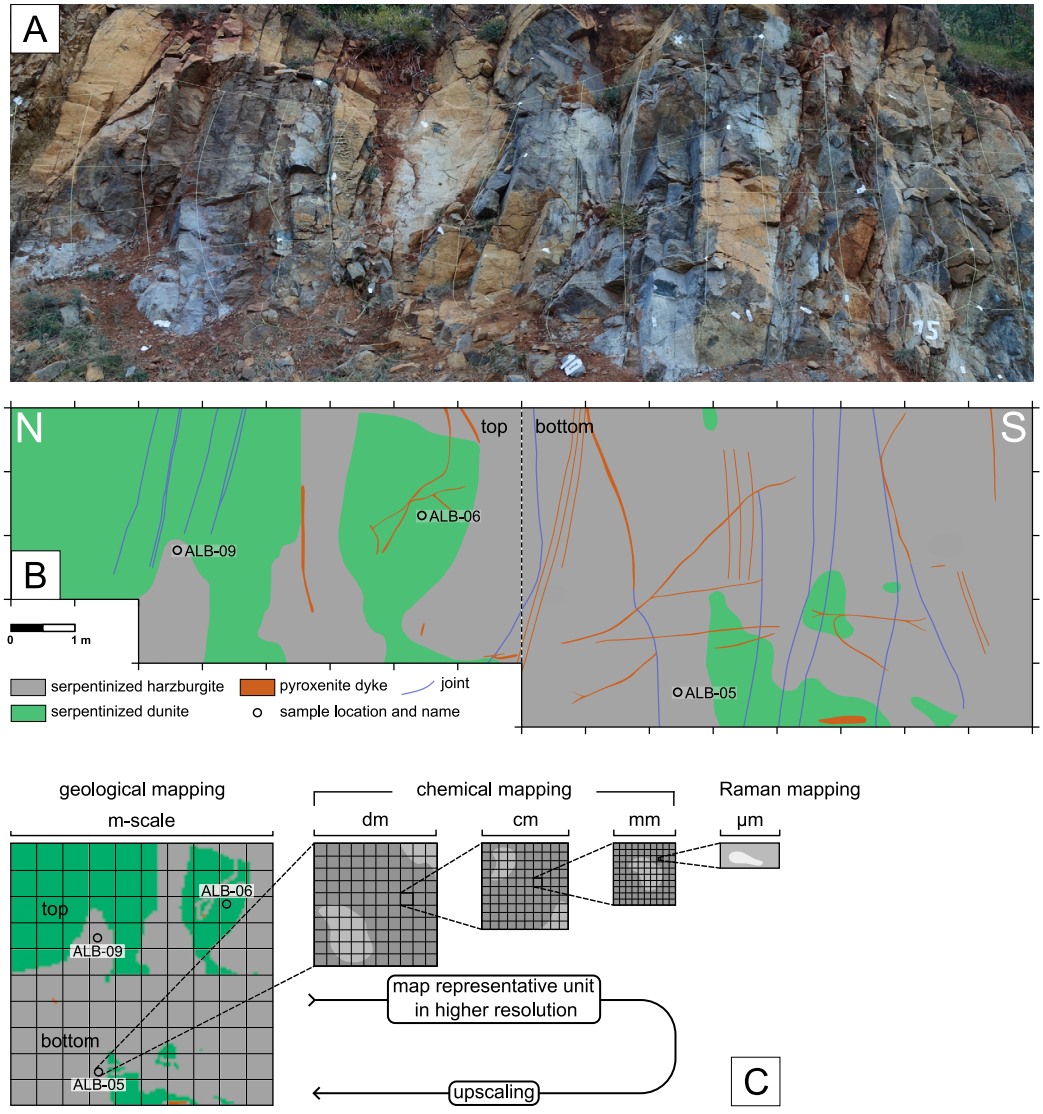

Fig. 2. (A, B) Photograph and geologic map of outcrop. (C) Approach to generate a multiscale dataset. Starting with field observations at the tens of meters scale, we identified representative units and examined them in more detail at the next smallest scale until we reached the submillimeter scale. For the meter scale, we rearranged the outcrop by stacking the northern half on top of the southern half (the vertical dashed line in B indicates where we separated the map, see Upscaling Methods). From the decimeter down to the millimeter scale, we performed chemical mapping with increasing resolutions toward smaller scales to capture chemical heterogeneities. For the submillimeter scale, we performed Raman mapping. At the submillimeter scale, we then upscaled our results by homogenization to finally reach the meter scale again (see Upscaling Methods).

Frost (2021) and added an ideal solution model for lizardite. To generate the lizardite iron endmember, we used the reaction Fe-lizardite = Fe-talc + 3 Fe-brucite, assuming $\Delta H_r = 0$, as we are currently unaware of any thermodynamic data on this reaction. In the discussion, we address our choice of solution models and compare our results to those obtained when using the solution models of Holland and Powell (2004).

3.3.2. Slab Moho P-T path

We performed Gibbs free energy minimization for every composition in the 2D serpentinite domains along a distinct slab Moho P-T path from the compilation of Syracuse et al. (2010, P-T paths given in the appendix). We chose the Lesser Antilles P-T path for our calculations because it represents an intermediate P-T path and, therefore, is similar to many other subduction zone P-T paths worldwide. The subduction zone data are taken from the Supplementary Material of Syracuse et al. (2010, fig. 13), and pressure is calculated as lithostatic overburden pressure.

3.3.3. Porosity calculation

To study the effects of chemical heterogeneities on the timing and the amount of porosity production, we used eq. (1) to calculate porosity along the P-T path. This equation is based on the conservation of non-hydrous mass (Malvoisin et al., 2015), i.e., mass always bound to the solid, and has been successfully applied in previous studies, such as Plümper et al. (2017); Beinlich et al. (2020); Huber et al. (2022). In our system, with H_2O being the only fluid mobile component, the non-volatile density was calculated as $\rho_s(1 - X_{H_2O})$, with ρ_s and X_{H_2O} obtained from the post-processing of the Gibbs free energy minimization results, with ρ_s and X_{H_2O} being the solid density and the rock-bound water content, respectively. Equation (1) accounts for porosity formation by densification of the solid during dehydration without considering mechanical effects, such as compaction, or metasomatic effects, such as reactive fluid flow.

$$\phi = 1 - \frac{\rho_s^0(1 - X_{H_2O}^0)(1 - \phi^0)}{\rho_s(1 - X_{H_2O})} \quad (1)$$

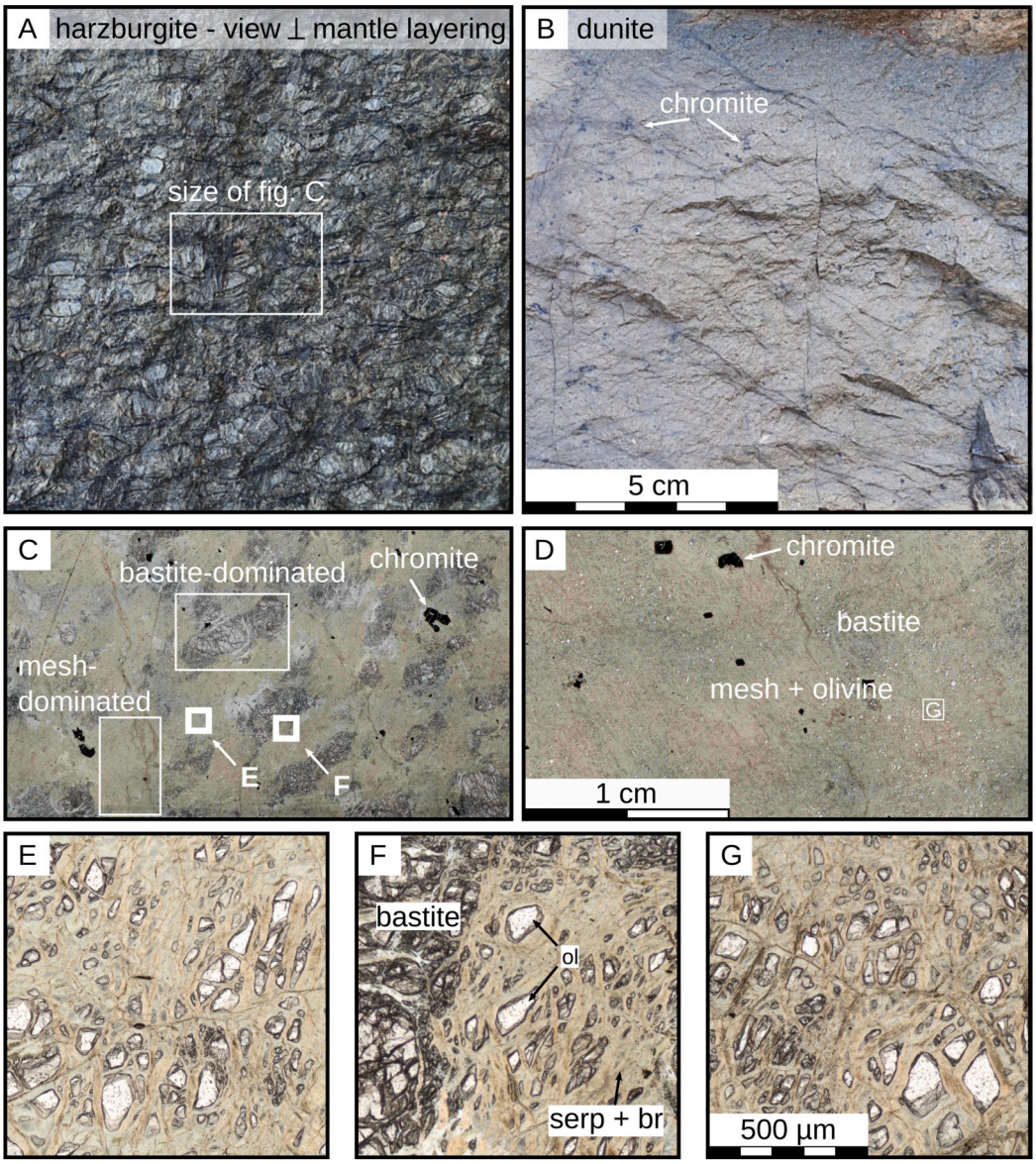

Fig. 3. Representative field images and textures found in serpentinized harzburgites and dunites in the outcrop. (A) Bastite-rich layer, resulting from high-T mantle layering. (B) Serpentinized dunite with chromite pods. (C, D) Thin sections of serpentinized harzburgite and dunite, respectively. (E, G) Mesh texture in serpentinized harzburgite and dunite, respectively, with remnants of mantle olivine. (F) Contact between bastite and mesh texture in serpentinized harzburgite.

The superscript 0 refers to the reference point for the background porosity ϕ^0, which we set to zero before the first dehydration reaction occurs.

4. Results

4.1. Sample characteristics at various scales

The bulk part of the outcrop consists of serpentinized harzburgite including a significant volume of serpentinized dunite. Both lithologies have undergone almost complete serpentinization, but we use the terminology based on the precursor rock because this difference matters for our study. Dunite occurs as lenses within harzburgite, often reaching sizes of several meters or more (Fig. 2B). For example, near the outcrop, the entire section above the tunnel portal consists of a single dunite lens about 20 m in diameter. Both harzburgites and dunites are cut by pyroxenite dykes with centimeter-sized pyroxene crystals, most of which are altered to bastites. Bortolotti et al. (1996) recognized an increasing dunite content toward the Moho in their geological map of the ophiolite, and the presence of significant amounts of dunite is considered to indicate proximity to the petrological Moho (e.g., Morishita et al., 2011, and references therein), which in our case lies about 3 km further to the southwest (Fig. 1). The presence of dunite and harzburgites represents a first-order chemical heterogeneity on the kilometer scale of the Mirdita ophiolite (Bortolotti et al., 1996) down to the meter scale of our outcrop. A similar pattern emerges on the decimeter scale and is visible in the field photographs (Fig. 3). The view of a fresh harzburgite surface (Fig. 3A), taken perpendicular to the mantle layering, shows the abundance of pyroxenes oriented along the primary mantle layering. Such pyroxene-rich layers are absent in the dunite (Fig. 3B), which appears more homogeneous at the decimeter scale compared to the harzburgite.

Zooming further in reveals that the same principal heterogeneity is also present on the centimeter scale (Fig. 3C, D). In Fig. 3, panels C and D show thin-section photographs of a representative sample of harzburgite and dunite, respectively. On the millimeter scale, some domains in the harzburgite are dominated by bastites, others by mesh texture only, as highlighted by the white boxes in Fig. 3C. In contrast, all millimeter-scale domains in the dunite are dominated by mesh textures. A direct comparison of the millimeter-scale textures shows the textural similarity

Table 1
Mineral chemical data of mesh texture and main minerals found in our samples. Values are mean values of the single measurements given in the Supplementary Information. H = harzburgite, D = dunite with the number of measurements considered given in parentheses.

	Mesh (Srp.+Brc.)		Serpentine		Olivine		Cpx		Opx
	H (17)	*D (17)*	*H (18)*	*D (10)*	*H (17)*	*D (17)*	*H (15)*	*D (3)*	*H (18)*
SiO_2	32.11	30.28	38.42	38.06	41.00	40.74	54.14	54.03	56.92
MgO	41.23	41.39	35.22	39.23	49.98	49.86	17.84	17.38	34.52
FeO	8.03	8.83	6.18	4.95	8.65	8.85	1.78	1.40	5.64
CaO	0.10	0.10	0.47	0.09	0.03	0.06	24.29	25.39	0.74
Cr_2O_3			0.29			0.01	0.40	0.29	0.42
Al_2O_3			0.49				0.75	0.60	0.89
TiO_2			0.01	0.01			0.01	0.02	0.01
Na_2O	0.04	0.04	0.03	0.02	0.01		0.08	0.08	0.01
K_2O			0.02					0.01	
MnO	0.09	0.11	0.19	0.07	0.12	0.13	0.07	0.02	0.13
Total	*81.6*	*80.75*	*81.32*	*82.43*	*99.79*	*99.65*	*99.36*	*99.22*	*99.28*
atoms per unit formula, normalized to the number of oxygens given in the last row									
Si	2.18	2.10	2.53	2.47	1.00	1.00	1.98	1.98	1.97
Mg	4.17	4.28	3.46	3.79	1.82	1.82	0.97	0.95	1.78
Fe	0.46	0.51	0.34	0.27	0.18	0.18	0.05	0.04	0.16
Ca	0.01	0.01	0.03	0.01	0.00	0.00	0.95	1.00	0.03
Cr	0.00	0.00	0.01	0.00	0.00	0.00	0.01	0.00	0.01
Al	0.00	0.00	0.02	0.00	0.00	0.00	0.02	0.01	0.02
Ti	0.00	0.00	0.00	0.00	0.00	0.00	0.00	0.00	0.00
Na	0.00	0.00	0.00	0.00	0.00	0.00	0.00	0.00	0.00
K	0.00	0.00	0.00	0.00	0.00	0.00	0.00	0.00	0.00
Mn	0.01	0.01	0.01	0.00	0.00	0.00	0.00	0.00	0.00
O	14.00	14.00	14.00	14.00	4.00	4.00	6.00	6.00	6.00

between mesh textures in harzburgite and dunite (Fig. 3E and 3G, respectively). However, a clear textural difference is visible between mesh textures and bastite (Fig. 3F).

4.1.1. Mineral chemical data

The information we could extract from mesh textures below the millimeter scale using optical microscopy is limited. To obtain further information about chemical heterogeneities and differences in the mineral chemistry between both lithologies, we performed chemical mappings and quantitative point analysis on individual minerals; Table 1 shows representative results. We provide a complete list of all microprobe data in the Supplementary Information.

The characteristic of the mesh texture is the serpentine mineral with intergrown brucite (Fig. 4). Our measurements show two main compositional differences between the two lithologies. Mesh textures in dunites contain about 2 wt.% less SiO_2 and are slightly FeO richer than the textural equivalent mesh textures in harzburgites (Table 1). The second main difference is the MgO content of serpentine. Dunite serpentine is MgO richer (about 4 wt.%) and FeO poorer (about 1.2 wt.%) than serpentine minerals in the harzburgite sample.

The occurrence of clinopyroxene (Cpx)-bastites near some measurement points can explain the 0.47 wt.% CaO in harzburgite serpentines. The composition of remnant mantle olivines is similar in both lithologies, with FeO contents of about 8-9 wt.%, which is typical for mantle olivines. Orthopyroxenes (Opx) are abundant in harzburgite and are often heavily altered to talc and serpentine (bastites). The contact zone between bastites and mesh textures usually consists of pure serpentine due to the transition from relatively high SiO_2 in bastites to lower SiO_2 contents in the mesh texture. Clinopyroxenes (Cpx) are more common in harzburgites and only occur as small remnants in dunites. The number of Cpx measurements in dunites is limited to only three; no significant compositional differences exist between Cpx in harzburgites and dunites.

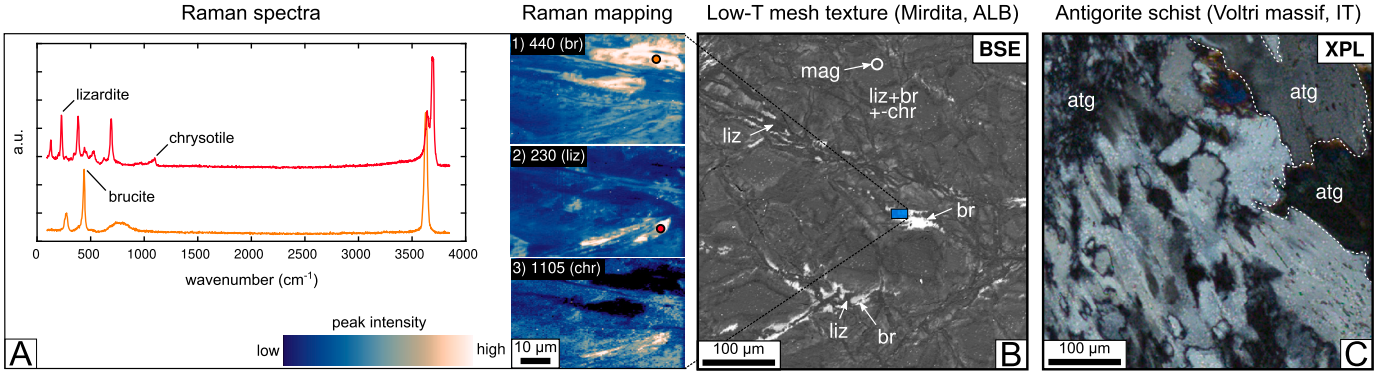

Fig. 4. Results of (A) Raman mapping and (B, C) mineralogical and textural changes during the lizardite-antigorite transition. (A) Two representative spectra whose positions on the map are shown on the right (Panels 1, 2) by two circles in corresponding colors. Panels 1-3 show the peak intensities for brucite (440 cm), lizardite (230 cm), and chrysotile (1105 cm), respectively. Chrysotile occurs only in minor amounts along with lizardite, typically filling up voids during the final stages of serpentinization (Evans, 2004). (B) BSE image of a typical low-temperature mesh texture (sample ALB06-2) found in both harzburgites and dunites (Fig. 3E, G). The blue box highlights the Raman mapping area. The single brucite flakes are typically iron rich and preferably occur along veins of pure lizardite, commonly interpreted as the result of a multistage serpentinization process. (C) Crossed polarizers photomicrograph of an antigorite schist (courtesy of E. Schwarzenbach) with typical interlocking texture, showing the effect of grain coarsening after the lizardite-antigorite transition. BSE = backscattered electron, XPL = crossed polarizers.

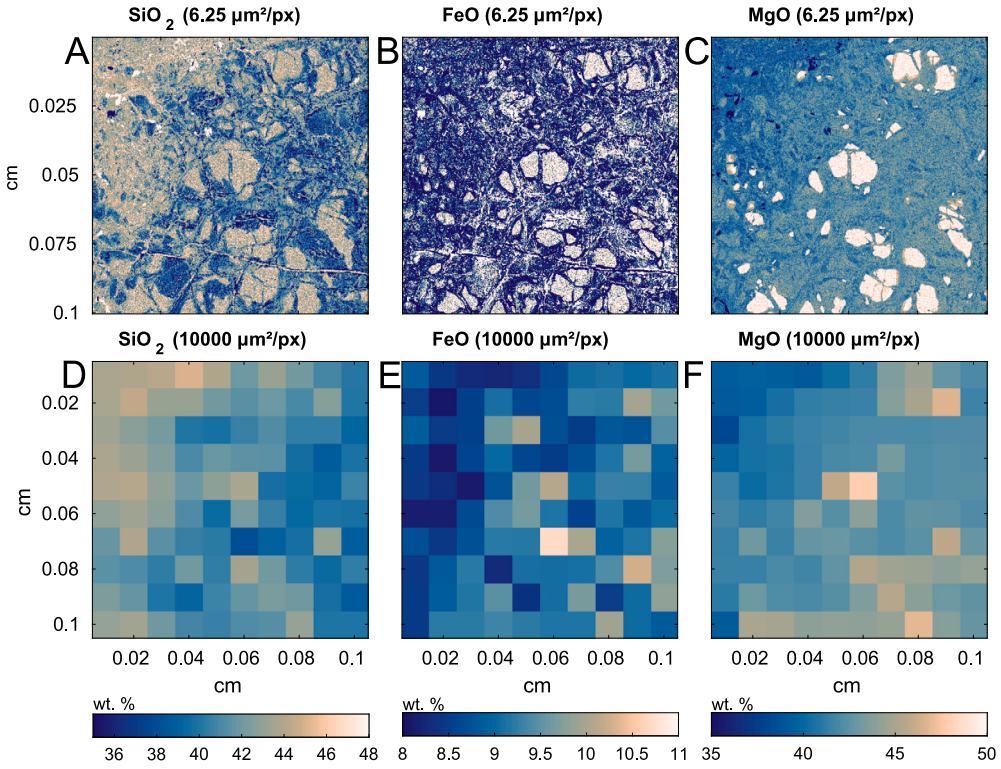

Fig. 5. Element distribution mappings for an area of 1 mm^2 in sample ALB05 (serpentinized harzburgite). Top (A-C): Original maps with a step size of 2.5 µm (or 6.25 $µm^2$/pixel). Bottom (D-F): Coarsened maps with a step size of 100 µm, which is equivalent to 100,000 $µm^2$/pixel. The map covers a bastite-dominated part (top left) and a mesh texture-dominated part (lower right) with remnant mantle olivines (visible at high Mg contents). The coarsened maps preserve the primary chemical heterogeneities. All plots in a row and column share the same y- and x-axis, respectively. Each component's original and coarse maps share the same color bar.

4.2. Grain coarsening during the lizardite-antigorite transition

The minerals' chemical data show that the mesh texture has a significantly lower SiO_2 content than areas consisting of pure serpentine minerals, which are present in bastites (along with talc) or in veins cutting the mesh texture (Fig. 4B). SiO_2 contents of less than ~42 wt.% are insufficient to form pure serpentine and may result in the formation of fine-grained (< 1 µm) intergrown brucite. Brucite also commonly occurs as single crystals in both lithologies and is visible in backscattered electron images due to its typically high iron content (Fig. 4B). To confirm the presence of brucite within the mesh texture, we performed Raman spectroscopy mapping in the area depicted by the blue box in Fig. 4B. The results of Raman mapping and two representative Raman spectra are shown in Fig. 4A. The two circles on the map indicate the location of the two spectra, showing the representative peaks for lizardite and chrysotile (top spectrum), and brucite (bottom). Panels 1-3 in Fig. 4A show the spatial distribution of the peak intensity for each of these three peaks.

Our Raman mapping results confirm that the mesh texture consists mainly of a mixture of lizardite and brucite along with minor amounts of chrysotile. Accordingly, varying contents of iron-rich brucite lead to the more subtle brightness differences in Fig. 4B in the mesh texture, with brighter gray tones indicating higher brucite content. Panel B of Fig. 4 also shows veins of pure serpentine cutting through the mesh texture. These veins are common in serpentinites and are interpreted as the result of a multistage serpentinization process (e.g., Evans and Frost, 2021). In our samples, fine-grained magnetite is distributed in the mesh texture (Fig. 4B). This texture is interpreted as the result of serpentinization below ~200 °C, while magnetite concentrated in the center of serpentinization veins indicates serpentinization between 200 and 300 °C (Bach et al., 2006).

During the onset of subduction and with increasing P-T conditions, lizardite and chrysotile transform into antigorite during the lizardite-antigorite transition, which Schwartz et al. (2013) report to occur at temperatures between 300 and 390 °C. Antigorite overgrows the previous fine-grained texture and forms an interlocking or interpenetrating texture of coarser antigorite blades. In Fig. 4C, which shows a crossed polarizer photomicrograph of an antigorite schist from the Voltri Massif in Liguria, Italy, a complete lizardite-antigorite transition is displayed, but the sample has not yet experienced P-T conditions high enough for dehydration to begin. As such, the textural difference between Fig. 4B and C must be considered when studying the effects of chemical heterogeneities on dehydration dynamics, because, at the time of dehydration onset at depth, the coarser antigorite texture will most likely have already replaced the low-temperature mesh texture.

Antigorite growth is accompanied not only by textural but also by chemical changes. The growth of antigorite flakes leads to a local homogenization, overprinting the previous submicron- to micron-scale chemical heterogeneities (see also Evans et al., 2013). To account for the grain coarsening and the local homogenization, we added coarsening and local homogenization to our millimeter-scale chemical maps (Fig. 5). Note that each of the 10×10 pixels of the coarse map (Fig. 5D-F) are modeled following the P-T path (Fig. 6).

A second chemical effect during the lizardite-antigorite transition is attributed to the slightly higher SiO_2 content of antigorite compared to lizardite. Antigorite may form by one of the following two reactions: (1) liz/chr + SiO_2(aq) = atg or (2) liz/chr = atg + br (e.g., Evans, 2004). Reaction 1 occurs at least locally in an open system where an external fluid adds SiO_2, whereas reaction 2 occurs in a closed system with additional brucite growth during the transition. As we performed our thermodynamic calculations in a closed system, the results of our calculations show increasing brucite abundance during the lizardite-antigorite transition according to reaction 2 (Fig. 6).

4.3. Chemical heterogeneities on millimeter scales

We started our investigations with representative mapping on the millimeter scale. Here, Fig. 5 shows the distribution of SiO_2, MgO, and FeO, the main elements of interest for our thermodynamic calculations. The top row of Fig. 5 (A-C) shows the original maps with size 1×1 mm with a step size of 2.5 µm, i.e., every pixel covers an area of 6.25 μm^2. Two distinct domains are visible in the SiO_2 and MgO distributions. The upper left parts of the maps consist of serpentine, characterized by relatively high SiO_2 and low MgO contents. Toward the bottom right corners, the maps consist of mesh texture, visible by lower SiO_2 and higher FeO contents, attributed to brucite. Spots with the highest MgO contents are remnant mantle olivine grains. The bottom row of Fig. 5 (D-F) shows the coarsened maps with 10×10 pixels, i.e., each pixel now covers an area of 10,000 mm^2. Each pixel in the coarsened maps reflects the average composition of 1600 pixels (40×40) in the original maps. The result is an overall more homogeneous material and a loss of information about the chemical variability, but the coarsened maps still preserve the primary information about the presence of a bastite-dominated part and a mesh texture-dominated part.

4.4. Metamorphic evolution along the P-T path

The chemical heterogeneities in the coarse millimeter-scale chemical maps affect the spatial distribution of the initial stable mineral assemblage at the first point of the P-T path and the subsequent metamorphic evolution. Panel A of Fig. 6 shows the P-T path used in our calculations, with three boxes highlighting the main events during dehydration. First, the lizardite-antigorite transition at temperatures below ~350 °C; second, the onset of dehydration as defined by the first occurrence of a non-hydrous phase (Ol or Opx); and, third, the subsequent porosity evolution due to dehydration reactions.

In Fig. 6B and 6C, we show the evolution of the stable mineral assemblage for the coarse-mapped pixel with the lowest and highest temperature of dehydration onset, respectively. The bulk rock composition for the mineral assemblage shown in Fig. 6B contains more SiO_2 than the bulk composition of Fig. 6C, which stabilizes antigorite over lizardite and brucite at lower P-T conditions. Because we performed our thermodynamic calculations in a closed system, additional brucite formed in both Fig. 6B and Fig. 6C during the lizardite-antigorite transition. The dehydration onset, marked by the occurrence of the first metamorphic olivine, was at 498 °C in the SiO_2-richer composition (Fig. 6B), compared to 520 °C in the SiO_2-poorer domain (Fig. 6C). The higher brucite abundance in Fig. 6C led to more antigorite consumption in the brucite-out reaction and, thus, a larger decrease in solid-bound H_2O. The SiO_2-richer domain retained more antigorite until the antigorite-out reaction started at ~580 °C. Therefore, this second dehydration reaction was more pronounced in the SiO_2-richer domain. Our results show that dehydration starts in parts of the rock with a relatively high SiO_2 and FeO content. However, these domains will retain more solid-bound H_2O in antigorite until the antigorite-out reaction, whereas SiO_2-poorer parts of the rock, with a later dehydration onset, release more H_2O with the brucite-out reaction.

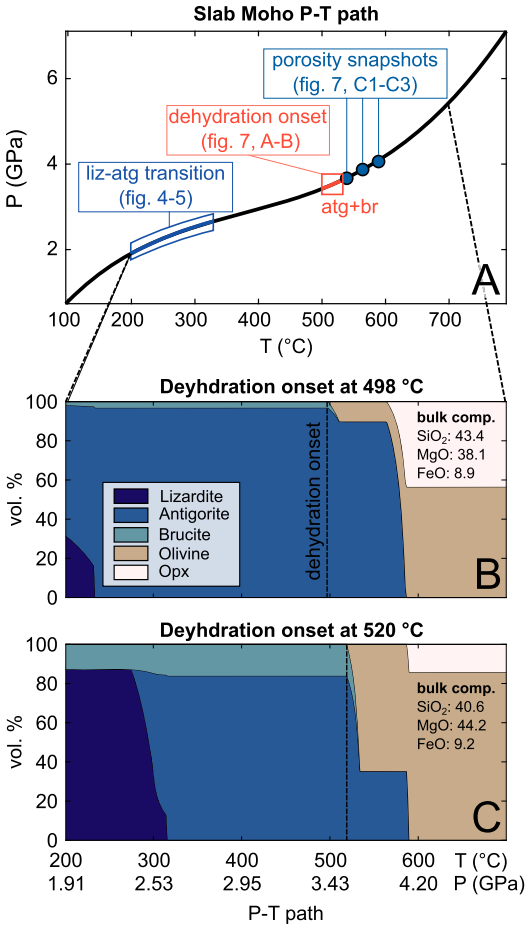

Fig. 6. (A) Slab Moho P-T path with a blue and red box highlighting the P-T range for the lizardite-antigorite transition and the onset of dehydration, respectively. Blue circles indicate the P-T conditions of the porosity snapshots in Fig. 7C. (B, C) Evolution of mineral assemblage along the P-T path for the domain in the coarse map with (B) the lowest and (C) the highest temperature for dehydration onset, as marked by the vertical dashed line. Bulk compositions are given in wt.%.

5. Discussion

5.1. Effects of local variations in FeO and SiO_2 abundance

Compared to other rock types undergoing dehydration during subduction, serpentinites have a relatively simple chemistry, making them an ideal lithology for studying the effects of chemical variations on dehydration dynamics through single-component exploration. In the FMSH system, the local FeO and SiO_2 contents control both the temperature of the dehydration onset and the extent of each of the two subsequent dehydration reactions (and, thus, the porosity evolution) while dehydration proceeds. At low P-T conditions, SiO_2 abundance governs brucite stability and, thus, the extent of the brucite-out reaction (Fig. 6B, C). A higher FeO abundance leads to Fe-richer compositions of ferromagnesian silicates, which react at lower temperatures than their Mg-richer equivalents. Thus, higher FeO contents extend the divariant field of the dehydration reaction toward lower temperatures.

We show the combined effects of SiO_2 and FeO abundance on the dehydration onset in Fig. 7A, which displays the molar Si ratios of all pixels in the coarse millimeter-scale maps against molar Fe ratios. The colors filling the circles indicate the temperature for the dehydration onset as defined by the first occurrence of a metamorphic non-hydrous phase. The figure shows that the temperatures of dehydration onset decrease upon increasing molar Si/Fe ratios. The spatial distribution of the dehydration onset temperature (Fig. 7B) and three snapshots of the spatial porosity distribution (Fig. 7C) also show the correlation between porosity and the spatial distribution of SiO_2 and FeO in the coarse maps (Fig. 5). This figure also demonstrates that domains with a higher SiO_2 and FeO content form the first porosity (Fig. 7B, C1), whereas the SiO_2-poorer regions produce more porosity during the brucite-out reaction (Fig. 7C2). At P-T conditions above the terminal antigorite-out reaction (Fig. 7C3), all pixels have similarly high values for the cumulative porosity of around 0.3.

The choice of solution models has a significant impact on the results. We used the solution models of Evans and Frost (2021), as the results of the calculations are in good agreement with experimental data (e.g.,

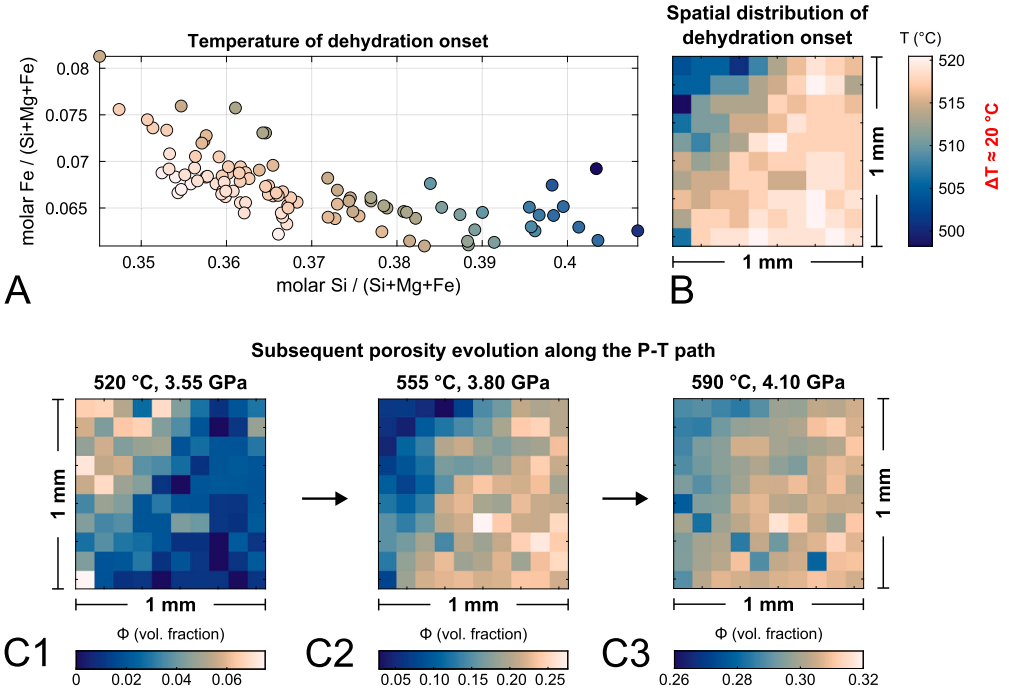

Fig. 7. (A) Effect of bulk Si and Fe variations (molar ratios) on the temperature of dehydration onset and subsequent porosity evolution. (B) Spatial distribution of dehydration onset. The part of the map with the highest molar Si and Fe ratio dehydrates first (top left). (C) Spatial porosity snapshots along the P-T path after (C1) the onset of dehydration until (C3) the end of the antigorite-out reaction. P-T conditions of snapshots C1-C3 are shown by blue circles on the P-T path in Fig. 6A. Note that the range of ϕ varies in each color bar of C1-C3.

Padrón-Navarta et al., 2011, 2013). In addition, we performed the same calculations using the Holland et al. (2018) solution models, and we found that olivine is stable at temperatures as low as 200 °C, or already at the beginning of the P-T path. Brucite consumption by the brucite-out reaction starts at around 400 °C, thus about 100 °C lower than in the results presented in Fig. 7. The reason for olivine stability at such low temperatures is the fayalite-rich olivine compositions with Mg-numbers of around 0.04 using the solution models of Holland et al. (2018). In comparison, the Evans and Frost (2021) solution models result in Mg-numbers for the first stable olivine of ~0.7, which is in better agreement with our measured olivine compositions (Table 1). The appendix contains a figure that compares the results of both solution models.

To investigate a potential scale dependence of the spatio-temporal fluid production during slab dehydration, we calculated the cumulative fluid release and the time-dependent fluid production over five orders of magnitude, from the millimeter scale to the outcrop scale (Fig. 8). The top row of Fig. 8 shows the evolution of cumulative fluid release for the domain with the earliest, the mean, and the latest dehydration onset on each scale (blue, red, and yellow graphs, respectively). The figure shows that the later the brucite-out reaction starts, the more fluid it liberates, while the opposite trend occurs for the antigorite-out reaction.

5.2. Fluid production comparison across all scales

To investigate a potential scale dependence of the spatio-temporal fluid production during slab dehydration, we calculated the cumulative fluid release and the time-dependent fluid production over five orders of magnitude, from the millimeter scale to the outcrop scale (Fig. 8). The top row of Fig. 8 shows the evolution of cumulative fluid release for the domain with the earliest, the mean, and the latest dehydration onset on each scale (blue, red, and yellow graphs, respectively). The figure shows that the later the brucite-out reaction starts, the more fluid it liberates, while the opposite trend occurs for the antigorite-out reaction.

In the middle row of Fig. 8, we show the fluid production between two steps along the P-T path. The graphs in the middle row represent the first derivative of the curves in the top row with respect to time. Every graph shows two distinct peaks corresponding to the two dehydration reactions. We calculated time intervals by calculating the vertical slab velocity and assuming lithostatic pressure to calculate the time between two points along the P-T path. For the depicted P-T path, we used a convergence rate of 17.9 km/Ma and a subduction angle of 42.4°, as given in Syracuse et al. (2010), and a mantle density of 3300 kg m^{-3}. Under these assumptions, the 20 °C difference in the temperature for the dehydration onset corresponds to a time difference of about 0.3 Ma, or less than 4 km depth. The complete brucite-out reaction within the millimeter-scale domain would occur over 0.6 Ma (or 9 km), compared to about 0.7 Ma for the antigorite-out reaction. The fluid production evolution demonstrates that similar peaks of fluid production occur over five orders of magnitude of length scales. The peak distribution shows that fluid production during subduction occurs in scale-independent pulses, which vary in time and space due to the intrinsic chemical heterogeneities of the slab. The results of our fluid release calculation show that a coherently similar pattern for the production emerges across all scales due to the highly similar patterns in SiO_2 and FeO abundance on every scale. On the millimeter to centimeter scale, these differences in SiO_2 and FeO availability emerge as mesh texture and bastites, i.e., textural differences. On the meter or even kilometer scale, these chemical differences manifest as different lithologies such as dunite, harzburgite, or pyroxenite and their intrinsic chemical heterogeneities (e.g., Bortolotti et al., 1996; Niu, 2004; Peters et al., 2020).

5.3. Effects of extension to FMSHO and FMASH systems

For simplicity, we performed all our thermodynamic calculations in the FMSH system, as it allows for exploring the effects of the principal dehydration reactions systematically. However, serpentinization is often accompanied by the formation of various amounts of magnetite, which may occur localized along veins or more disseminated in other cases (Bach et al., 2006; Schwarzenbach et al., 2016; Klein et al., 2014; Evans and Frost, 2021). This suggests that serpentinites are to some extent oxidized, although it is difficult to accurately estimate both the extent of

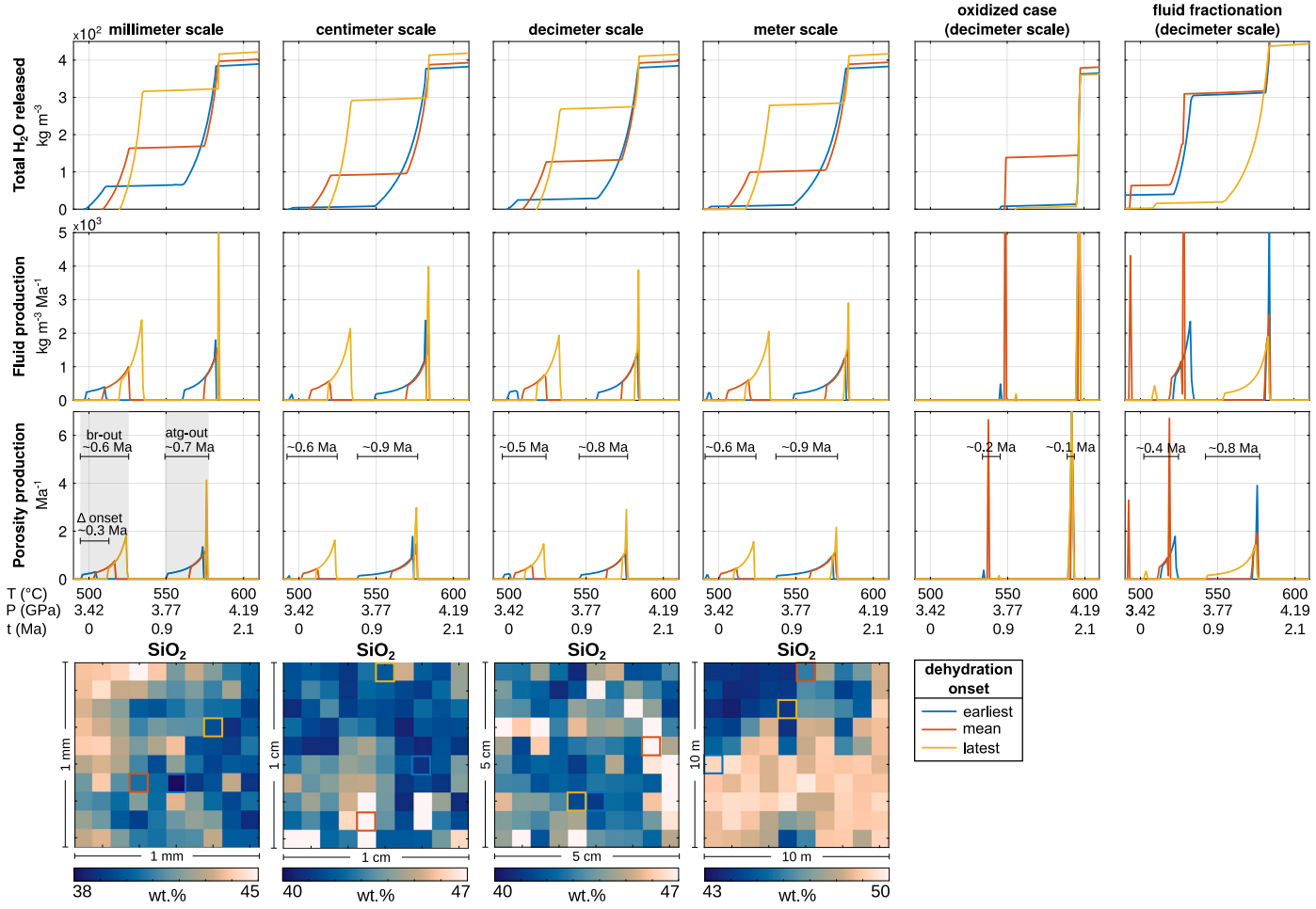

Fig. 8. Comparison of fluid production evolution along the P-T path across all scales considered in this study, focusing on domains with the lowest, mean, and highest temperatures of dehydration onset in case of a reduced bulk composition without fluid fractionation. Time (t) is calculated for the Antilles subduction zone, assuming lithostatic pressure, a subduction angle of 42.4°, a mantle density of 3300 kg m^{-3}, and a subduction rate of 17.9 km/Ma (Syracuse et al., 2010). The effects of an oxidized bulk composition and complete fluid fractionation after each P-T step are shown in columns four and five, respectively. Top row: total H_2O released; center and bottom row: fluid and porosity production per Ma, respectively; lowermost row: heterogeneous SiO_2 distribution at each scale. Colored boxes highlight the domains whose evolution is depicted in the plots above. Note that all chemical maps have a range of 7 wt.% with different minimum and maximum values.

oxidation and the spatial extent of variability, especially when departing from the thin-section scale (e.g., Evans and Frost, 2021).

Extending the chemical system to FMSHO has been done for a very oxidized case, where approximately two-thirds of the total Fe is ferric (i.e., Evans and Frost, 2021). For our decimeter scale, which already considers a larger degree of chemical homogenization, such a highly oxidized system leads to an onset of dehydration at a higher temperature, at about 550 °C for the earliest start (Fig. 8). The related divariant field is very narrow, as only about 4.4 vol.% of rather Mg-rich brucite formed because a significant portion Fe is bound in magnetite (approx. 4.6 vol.%), also causing lower Fe/Mg ratios in silicates (see also Trommsdorff and Evans, 1972; Evans and Frost, 2021). A second pulse of fluid release occurs at about 595 °C which reflects the terminal antigorite-out reaction, which again is characterized by a narrow divariant field as the antigorite composition is close to the Mg endmember (Fig. 8). These findings indicate that for highly oxidized cases, the fluid production occurs at minuscule T intervals and, thus, in short pulses (approx. 0.2 Ma for the brucite-out reaction), with almost the entire fluid release being connected to the terminal antigorite-out reaction. Consequently, higher oxygen fugacities increase temperatures for the onset of dehydration by decreasing the temperature intervals of the divalent fluid-releasing reactions.

Extending the chemical system to FMASH creates new divariant fields by stabilizing chlorite and, at high P-T conditions, garnet (Padrón-Navarta et al., 2013; Evans and Frost, 2021). Chlorite is an important carrier of solid-bound water to sub-arc depths and is the last hydrous phase to break down during prograde metamorphism. Considering chlorite formation in our calculations would lower the magnitude of the first two peaks for porosity production and result in a third peak at about 770 °C, after the terminus of the antigorite-out reaction. Including Al_2O_3 allows for the incorporation of Al in antigorite, which widens the divariant field of the antigorite-out reaction (Padrón-Navarta et al., 2013). Thus, Al in antigorite has a similar effect as Fe-Mg substitution, which the FMSH system can reflect. Padrón-Navarta et al. (2013) note that the divariant fields in the FMASH system widen compared to in the FMSH system, which would result in less pronounced peaks in our porosity evolution curves (Fig. 8). As Evans and Frost (2021) note, highly oxidized serpentinites are probably rather rare, and while the spatial distribution of the different degrees of serpentinite oxidation is in principle unknown, it is certainly heterogeneous. The low aluminum contents in our samples suggest that aluminum is also heterogeneously distributed within the slab mantle (e.g., Niu, 2004; Peters et al., 2020), contributing to the mantle's chemical heterogeneity. Consequently, the third peak in porosity production will not occur in all parts of the slab. Al-bearing parts will retain water at the same depths for which Al-free parts will have undergone complete dehydration, whereas more oxidized parts will have shorter and more pronounced pulses of fluid release.

5.4. Porosity formation and percolation threshold

Our porosity calculation is based on densification of the solid phase and neglects deformation effects, most importantly compaction. Our calculations of porosity production (Fig. 8, bottom row) are conducted similarly to those of fluid production (Fig. 8, middle row): As the dehydration reactions cause densification of the bulk solid, porosity formation and fluid production display the same pulse-like pattern during the simulated subduction. The liberated fluid will fill the dynamically forming porosity and eventually flow along fluid pressure gradients within the porous network when the newly formed porosity reaches the percolation threshold. Thermodynamic and petrophysical modeling (Plümper et al., 2017) have shown that vein-like porosity structures are formed even at the onset of serpentinite dehydration, and vein networks related to slab mantle dehydration have been reported from several localities (Groppo and Compagnoni, 2007; Jabaloy-Sanchez et al., 2022; López Sánchez-Vizcaíno et al., 2009; Scambelluri et al., 1991; Herms et al., 2012; John et al., 2012; Spandler et al., 2011).

For such a vein-like porosity geometry, the percolation threshold is reached even for porosities below 0.1 vol.%, or 0.001 in volume fractions (Bloch et al., 2018). Accordingly, considering the non-spherical porosity shape in our domain (Fig. 7C), fluid flow within the porous network will likely start soon after the dehydration onset, and compaction will lead to a dynamic closing of the compliant porosity. Such a compaction-related deformation process would agree with a fluid-channeling process such as porosity waves (Connolly and Podladchikov, 2015; Yarushina and Podladchikov, 2015; Yarushina et al., 2022), which would accelerate the spatio-temporal pulse-like behavior of the slab fluid release (Tian et al., 2018; Piccoli et al., 2021; Wilson et al., 2017). Therefore, the peaks in our porosity- and fluid-production calculations suggest that chemical heterogeneities at all scales lead to fluid pulses through high-transient porosities localized in both space and time. The vein-like shape of the porosity and the high porosity production rates allow for efficient fluid transport within the porous network throughout slab dehydration.

5.5. Effects of H_2O fractionation

We performed our thermodynamic calculations without removing H_2O in the liberated fluid phase from the bulk composition. However, the elongated porosity shape shown in Fig. 7C likely facilitates fluid flow even at low porosities, effectively removing some H_2O in the liberated fluid phase from the local bulk composition. To evaluate the effects of fluid fractionation, we repeated the thermodynamic calculations for the decimeter scale with complete H_2O fractionation (Fig. 8). The comparison shows the system's scale-independent behavior with two main peaks for the brucite-out and antigorite-out reaction. With fractionation, the peak amplitudes increase and the peaks narrow, corresponding to a shorter reaction time span. The duration of the brucite-out reaction decreases from approximately 0.5 Ma without fractionation to approximately 0.4 Ma with fractionation. H_2O fractionation also affects the metamorphic evolution and significantly expands the P-T window for the onset of dehydration. SiO_2-richer domains form olivine at temperatures as low as 250 °C; in contrast, the highest temperature for the onset of dehydration occurs in a relatively SiO_2-poor domain at 520 °C, i.e., at conditions similar to the non-fractionated case.

6. Implications for slab fluid release

Self-similar silica and iron distribution patterns occur in serpentinites derived from harzburgitic or dunitic precursors over at least five spatial orders of magnitude. These intrinsic chemical heterogeneities manifest as differences between mesh texture and bastites on the millimeter and centimeter scales and as lithological contrasts between dunites, harzburgites, and pyroxenites on the outcrop and crustal scales. Our results show that fluid production within the slab occurs by spatially localized pulses rather than due to continuous pervasive dehydration fluid flow. Fluid pulses occur on the order of 0.5-0.9 Ma for reduced serpentinite bulk compositions and as short as 0.1 Ma for oxidized serpentinite bulk compositions (see colored lines in the grey areas of Fig. 8), and fluid production peaks when P-T conditions approach the stability limit of hydrous phases. Fluid pulse time spans are also shortened by 0.1-0.2 Ma in the case of continuous fluid fractionation (Fig. 8, 9), resembling high fluid fluxes, for example by hydrofracturing, once the percolation threshold is reached. Our finding on fluid pulses aligns with other studies revealing that fluid release from subduction slabs is episodic at various scales with durations on the order of thousands of years to months, using chronometric approaches such as bulk- or garnet-diffusion modeling of dehydrating rocks or related vein-network systems (John et al., 2012; Yokoyama et al., 2002; Dragovic et al., 2015; Taetz et al., 2018; Yoshida et al., 2023).

The porosity structure evolves during subduction by feeding new fluid-filled porosity structures from different domains of their fluid source regions (Fig. 9). In turn, the scale-independent chemical heterogeneities cause variations in the chemical composition of the released fluid, which is in thermodynamic equilibrium with the composition of the host rock (Huber et al., 2022). Reactive fluid flow in such transient high-porosity structures (e.g., John et al., 2012; Piccoli et al., 2021; Tian et al., 2018; Taetz et al., 2018) can locally lower the temperature for dehydration reactions by changing the local bulk composition in the rock (e.g., Huber et al., 2022). Zooming out from the millimeter to the outcrop scale, fluid production always occurs heterogeneously distributed (Fig. 9). This likely holds true for the entire slab mantle, considering the regional distribution of the lithologies within the ophiolite (Bortolotti et al., 2005). Thus, a heterogeneous, spatio-temporal distribution of fluid production should occur at every scale, both along the strike and along the dip of the subducting plate.

CRediT authorship contribution statement

Konstantin Huber: Writing – review & editing, Writing – original draft, Visualization, Validation, Software, Resources, Methodology, Investigation, Formal analysis, Data curation, Conceptualization. **Timm John:** Writing – review & editing, Validation, Supervision, Resources, Project administration, Methodology, Investigation, Funding acquisition, Conceptualization. **Johannes C. Vrijmoed:** Writing – review & editing, Validation, Supervision, Software, Resources, Methodology, Investigation, Funding acquisition, Formal analysis, Data curation, Conceptualization. **Jan Pleuger:** Writing – review & editing, Supervision, Resources, Investigation, Data curation, Conceptualization. **Xin Zhong:** Writing – review & editing, Visualization, Validation, Software, Methodology, Investigation, Data curation.

Declaration of competing interest

The authors declare that they have no known competing financial interests or personal relationships that could have appeared to influence the work reported in this paper.

Data availability

The Supplementary Information, the mineral chemical data, the Raman mapping data, the multiscale dataset, and the MATLAB codes used to compile it are available on Zenodo (doi: https://dx.doi.org/10.5281/zenodo.13226433).

Acknowledgements

This research was funded by the Deutsche Forschungsgemeinschaft (DFG) through grant CRC 1114 Scaling Cascades in Complex Systems, Project Number 235221301, Project C09 and Pl 534/3-1. The authors

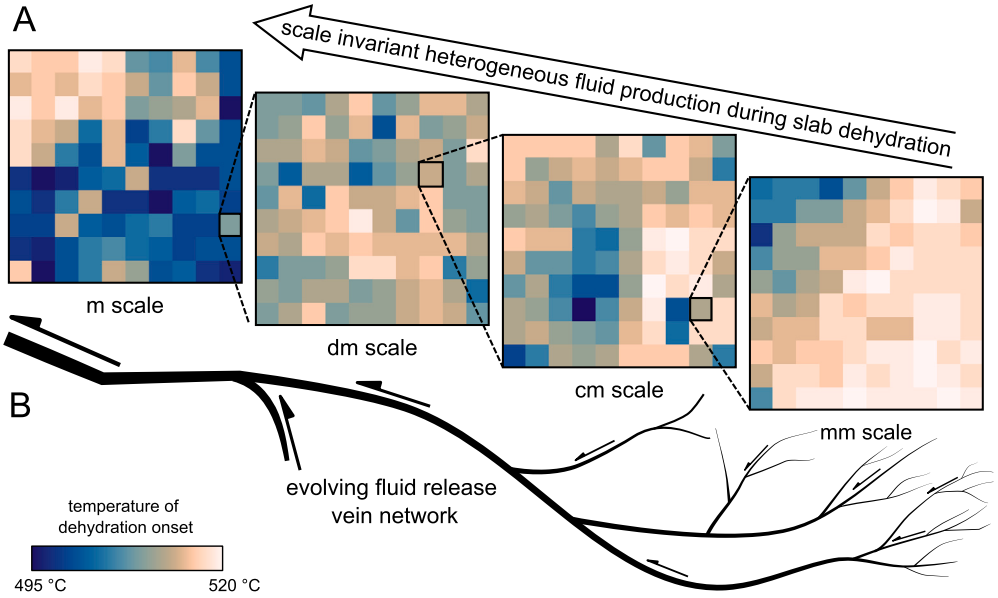

Fig. 9. Similar chemical heterogeneities from the millimeter up to the meter scale and beyond lead to scale-invariant fluid production. (A) Temperature of dehydration onset on all scales investigated in this study. Note that the plots share the same color bar. The appendix contains the same diagrams for all other scales for comparison. (B) Conceptual sketch of a dehydration vein network where dehydration starts at the millimeter scale and channelizes when going to larger scales. Arrows indicate the direction of fluid flow. Interpretation according to John et al. (2012); Plümper et al. (2017); John et al. (2008).

thank M. Scambelluri and E. Schwarzenbach for helpful discussions and for providing us with an antigorite schist sample. We would like to thank Celeste Brennecka for checking over an earlier version of the manuscript. The authors would also like to thank the two anonymous reviewers for their constructive criticism and Laurence Coogan for the good editorial handling, which together improved the quality of the study.

References

Ague, J.J., Tassara, S., Holycross, M.E., Li, J.L., Cottrell, E., Schwarzenbach, E.M., Fassoulas, C., John, T., 2022. Slab-derived devolatilization fluids oxidized by subducted metasedimentary rocks. Nat. Geosci. 15, 320–326. https://doi.org/10.1038/s41561-022-00904-7.

Bach, W., Paulick, H., Garrido, C.J., Ildefonse, B., Meurer, W.P., Humphris, S.E., 2006. Unraveling the sequence of serpentinization reactions: petrography, mineral chemistry, and petrophysics of serpentinites from MAR 15°N (ODP Leg 209, Site 1274). Geophys. Res. Lett. 33, L13306. https://doi.org/10.1029/2006GL025681.

Beinlich, A., John, T., Vrijmoed, J.C., Tominaga, M., Magna, T., Podladchikov, Y.Y., 2020. Instantaneous rock transformations in the deep crust driven by reactive fluid flow. Nat. Geosci. 13, 307–311. https://doi.org/10.1038/s41561-020-0554-9.

Bloch, W., John, T., Kummerow, J., Salazar, P., Krüger, O.S., Shapiro, S.A., 2018. Watching dehydration: seismic indication for transient fluid pathways in the oceanic mantle of the subducting nazca slab. Geochem. Geophys. Geosyst. 19, 3189–3207. https://doi.org/10.1029/2018GC007703.

Bortolotti, V., Korda, A., Marroni, M., Pandolfi, L., Faruk, M., Gianfranco, P., Saccani, E., 1996. Geology and petrology of ophiolitic sequences in Mirdita region (northern Albania). Ofioliti 21, 3–20.

Bortolotti, V., Marroni, M., Pandolfi, L., Principi, G., 2005. Mesozoic to Tertiary tectonic history of the Mirdita ophiolites, northern Albania. Isl. Arc 14, 471–493. https://doi.org/10.1111/j.1440-1738.2005.00479.x.

Brovarone, A.V., Butch, C.J., Ciappa, A., Cleaves, H.J., Elmaleh, A., Faccenda, M., Feineman, M., Hermann, J., Nestola, F., Cordone, A., Giovannelli, D., 2020. Let there be water: how hydration/dehydration reactions accompany key Earth and life processes. Am. Mineral. 105, 1152–1160. https://doi.org/10.2138/am-2020-7380.

Chen, S., Hin, R.C., John, T., Brooker, R., Bryan, B., Niu, Y., Elliott, T., 2019. Molybdenum systematics of subducted crust record reactive fluid flow from underlying slab serpentine dehydration. Nat. Commun. 10, 4773. https://doi.org/10.1038/s41467-019-12696-3.

Compagnoni, R., Cossio, R., Mellini, M., 2021. Raman anisotropy in serpentine minerals, with a caveat on identification. J. Raman Spectrosc. 52, 1334–1345. https://doi.org/10.1002/jrs.6128.

Connolly, J.A.D., Podladchikov, Y.Y., 2015. An analytical solution for solitary porosity waves: dynamic permeability and fluidization of nonlinear viscous and viscoplastic rock. Geofluids 15, 269–292. https://doi.org/10.1111/gfl.12110.

Dilek, Y., Furnes, H., Shallo, M., 2007. Suprasubduction zone ophiolite formation along the periphery of Mesozoic Gondwana. Gondwana Res. 11, 453–475. https://doi.org/10.1016/j.gr.2007.01.005.

Dilek, Y., Furnes, H., Shallo, M., 2008. Geochemistry of the Jurassic Mirdita Ophiolite (Albania) and the MORB to SSZ evolution of a marginal basin oceanic crust. Lithos 100, 174–209. https://doi.org/10.1016/j.lithos.2007.06.026.

Dragovic, B., Baxter, E.F., Caddick, M.J., 2015. Pulsed dehydration and garnet growth during subduction revealed by zoned garnet geochronology and thermodynamic modeling, Sifnos, Greece. Earth Planet. Sci. Lett. 413, 111–122. https://doi.org/10.1016/j.epsl.2014.12.024.

Elliott, T., Plank, T., Zindler, A., White, W., Bourdon, B., 1997. Element transport from slab to volcanic front at the Mariana arc. J. Geophys. Res., Solid Earth 102, 14991–15019. https://doi.org/10.1029/97JB00788.

Evans, B.W., 2004. The serpentinite multisystem revisited: chrysotile is metastable. Int. Geol. Rev. 46, 479–506. https://doi.org/10.2747/0020-6814.46.6.479.

Evans, K.A., Frost, B.R., 2021. Deserpentinization in subduction zones as a source of oxidation in arcs: a reality check. J. Petrol. 62, egab016. https://doi.org/10.1093/petrology/egab016.

Evans, K.A., Powell, R., Frost, B.R., 2013. Using equilibrium thermodynamics in the study of metasomatic alteration, illustrated by an application to serpentinites. Lithos 168–169, 67–84. https://doi.org/10.1016/j.lithos.2013.01.016.

Ferrand, T.P., Hilairet, N., Incel, S., Deldicque, D., Labrousse, L., Gasc, J., Renner, J., Wang, Y., Green II, H.W., Schubnel, A., 2017. Dehydration-driven stress transfer triggers intermediate-depth earthquakes. Nat. Commun. 8, 15247. https://doi.org/10.1038/ncomms15247.

Groppo, C., Compagnoni, R., 2007. Metamorphic veins from the serpentinites of the Piemonte Zone, western Alps, Italy: a review. Period. Mineral., 127–153. https://doi.org/10.2451/2007PM0021.

Groppo, C., Rinaudo, C., Cairo, S., Gastaldi, D., Compagnoni, R., 2006. Micro-Raman spectroscopy for a quick and reliable identification of serpentine minerals from ultramafics. Eur. J. Mineral. 18, 319–329. https://doi.org/10.1127/0935-1221/2006/0018-0319.

Hacker, B.R., Peacock, S.M., Abers, G.A., Holloway, S.D., 2003. Subduction factory 2. Are intermediate-depth earthquakes in subducting slabs linked to metamorphic dehydration reactions? J. Geophys. Res., Solid Earth 108. https://doi.org/10.1029/2001JB001129.

Herms, P., John, T., Bakker, R.J., Schenk, V., 2012. Evidence for channelized external fluid flow and element transfer in subducting slabs (Raspas Complex, Ecuador). Chem. Geol. 310–311, 79–96. https://doi.org/10.1016/j.chemgeo.2012.03.023.

Hirth, G., Guillot, S., 2013. Rheology and tectonic significance of serpentinite. Elements 9, 107–113. https://doi.org/10.2113/gselements.9.2.107.

Holland, T.J.B., Powell, R., 2004. An internally consistent thermodynamic data set for phases of petrological interest: an internally consistent thermodynamic data set. J. Metamorph. Geol. 16, 309–343. https://doi.org/10.1111/j.1525-1314.1998.00140.x.

Holland, T.J.B., Powell, R., 2011. An improved and extended internally consistent thermodynamic dataset for phases of petrological interest, involving a new equation of state for solids. J. Metamorph. Geol. 29, 333–383. https://doi.org/10.1111/j.1525-1314.2010.00923.x.

Holland, T.J.B., Green, E.C.R., Powell, R., 2018. Melting of peridotites through to granites: a simple thermodynamic model in the system KNCFMASHTOCr. J. Petrol. 59, 881–900. https://doi.org/10.1093/petrology/egy048.

Huber, K., Vrijmoed, J.C., John, T., 2022. Formation of olivine veins by reactive fluid flow in a dehydrating serpentinite. Geochem. Geophys. Geosyst. 23, e2021GC010267. https://doi.org/10.1029/2021GC010267.

Jabaloy-Sanchez, A., Sanchez-Vizcaino, V.L., Padron-Navarta, J.A., Hidas, K., Gomez-Pugnaire, M.T., Garrido, C.J., 2022. Olivine-rich veins in high-pressure serpentinites: a far-field paleo-stress snapshot during subduction. J. Struct. Geol. 163, 104721. https://doi.org/10.1016/j.jsg.2022.104721.

John, T., Klemd, R., Gao, J., Garbe-Schönberg, C.D., 2008. Trace-element mobilization in slabs due to non steady-state fluid–rock interaction: constraints from an eclogite-facies transport vein in blueschist (Tianshan, China). Lithos 103, 1–24. https://doi.org/10.1016/j.lithos.2007.09.005.

John, T., Gussone, N., Podladchikov, Y.Y., Bebout, G.E., Dohmen, R., Halama, R., Klemd, R., Magna, T., Seitz, H.M., 2012. Volcanic arcs fed by rapid pulsed fluid flow through subducting slabs. Nat. Geosci. 5, 489–492. https://doi.org/10.1038/ngeo1482.

Kempf, E.D., Hermann, J., Reusser, E., Baumgartner, L.P., Lanari, P., 2020. The role of the antigorite + brucite to olivine reaction in subducted serpentinites (Zermatt, Switzerland). Swiss J. Geosci. 113, 16. https://doi.org/10.1186/s00015-020-00368-0.

Klein, F., Bach, W., Humphris, S.E., Kahl, W.A., Jons, N., Moskowitz, B., Berquo, T.S., 2014. Magnetite in seafloor serpentinite–some like it hot. Geology 42, 135–138. https://doi.org/10.1130/G35068.1.

López Sánchez-Vizcaíno, V., Gómez-Pugnaire, M.T., Garrido, C.J., Padrón-Navarta, J.A., Mellini, M., 2009. Breakdown mechanisms of titanclinohumite in antigorite serpentinite (Cerro del Almirez massif, S. Spain): a petrological and TEM study. Lithos 107, 216–226. https://doi.org/10.1016/j.lithos.2008.10.008.

Malvoisin, B., Podladchikov, Y.Y., Vrijmoed, J.C., 2015. Coupling changes in densities and porosity to fluid pressure variations in reactive porous fluid flow: local thermodynamic equilibrium. Geochem. Geophys. Geosyst. 16, 4362–4387. https://doi.org/10.1002/2015GC006019.

Miller, S.A., van der Zee, W., Olgaard, D.L., Connolly, J.A.D., 2003. A fluid-pressure feedback model of dehydration reactions: experiments, modelling, and application to subduction zones. Tectonophysics 370, 241–251. https://doi.org/10.1016/S0040-1951(03)00189-6.

Morishita, T., Dilek, Y., Shallo, M., Tamura, A., Arai, S., 2011. Insight into the uppermost mantle section of a maturing arc: the Eastern Mirdita ophiolite, Albania. Lithos 124, 215–226. https://doi.org/10.1016/j.lithos.2010.10.003.

Nakagawa, T., Nakakuki, T., Iwamori, H., 2015. Water circulation and global mantle dynamics: insight from numerical modeling. Geochem. Geophys. Geosyst. 16, 1449–1464. https://doi.org/10.1002/2014GC005701.

Nicolas, A., Boudier, F., Meshi, A., 1999. Slow spreading accretion and mantle denudation in the Mirdita ophiolite (Albania). J. Geophys. Res., Solid Earth 104, 15155–15167. https://doi.org/10.1029/1999JB900126.

Niu, Y., 2004. Bulk-rock major and trace element compositions of abyssal peridotites: implications for mantle melting, melt extraction and post-melting processes beneath mid-ocean ridges. J. Petrol. 45, 2423–2458. https://doi.org/10.1093/petrology/egh068.

Padrón-Navarta, J.A., Tommasi, A., Garrido, C.J., Sánchez-Vizcaíno, V.L., Gómez-Pugnaire, M.T., Jabaloy, A., Vauchez, A., 2010. Fluid transfer into the wedge controlled by high-pressure hydrofracturing in the cold top-slab mantle. Earth Planet. Sci. Lett. 297, 271–286. https://doi.org/10.1016/j.epsl.2010.06.029.

Padrón-Navarta, J.A., López Sánchez-Vizcaíno, V., Garrido, C.J., Gómez-Pugnaire, M.T., 2011. Metamorphic record of high-pressure dehydration of antigorite serpentinite to chlorite harzburgite in a subduction setting (Cerro del Almirez, Nevado–Filábride Complex, Southern Spain). J. Petrol. 52, 2047–2078. https://doi.org/10.1093/petrology/egr039.

Padrón-Navarta, J.A., Sánchez-Vizcaíno, V.L., Hermann, J., Connolly, J.A., Garrido, C.J., Gómez-Pugnaire, M.T., Marchesi, C., 2013. Tschermak's substitution in antigorite and consequences for phase relations and water liberation in high-grade serpentinites. Lithos 178, 186–196. https://doi.org/10.1016/j.lithos.2013.02.001.

Peters, D., Pettke, T., John, T., Scambelluri, M., 2020. The role of brucite in water and element cycling during serpentinite subduction – insights from Erro Tobbio (Liguria, Italy). Lithos 360–361, 105431. https://doi.org/10.1016/j.lithos.2020.105431.

Piccoli, F., Ague, J.J., Chu, X., Tian, M., Vitale Brovarone, A., 2021. Field-based evidence for intra-slab high-permeability channel formation at eclogite-facies conditions during subduction. Geochem. Geophys. Geosyst. 22, e2020GC009520. https://doi.org/10.1029/2020GC009520.

Plümper, O., John, T., Podladchikov, Y.Y., Vrijmoed, J.C., Scambelluri, M., 2017. Fluid escape from subduction zones controlled by channel-forming reactive porosity. Nat. Geosci. 10, 150–156. https://doi.org/10.1038/ngeo2865.

Reynard, B., 2013. Serpentine in active subduction zones. Lithos 178, 171–185. https://doi.org/10.1016/j.lithos.2012.10.012.

Rüpke, L., Phipps Morgan, J., Eaby Dixon, J., 2006. Implications of subduction rehydration for Earth's deep water cycle. In: Jacobsen, S.D., Van Der Lee, S. (Eds.), Geophysical Monograph Series. American Geophysical Union, Washington, D.C., pp. 263–276.

Rüpke, L.H., Morgan, J.P., Hort, M., Connolly, J.A.D., 2004. Serpentine and the subduction zone water cycle. Earth Planet. Sci. Lett. 223, 17–34. https://doi.org/10.1016/j.epsl.2004.04.018.

Scambelluri, M., Strating, E.H.H., Piccardo, G.B., Vissers, R.L.M., Rampone, E., 1991. Alpine olivine- and titanian clinohumite-bearing assemblages in the Erro-Tobbio peridotite (Voltri Massif, NW Italy). J. Metamorph. Geol. 9, 79–91. https://doi.org/10.1111/j.1525-1314.1991.tb00505.x.

Schmid, S.M., Bernoulli, D., Fügenschuh, B., Matenco, L., Schefer, S., Schuster, R., Tischler, M., Ustaszewski, K., 2008. The Alpine-Carpathian-dinaridic orogenic system: correlation and evolution of tectonic units. Swiss J. Geosci. 101, 139–183. https://doi.org/10.1007/s00015-008-1247-3.

Schmidt, M.W., Poli, S., 1998. Experimentally based water budgets for dehydrating slabs and consequences for arc magma generation. Earth Planet. Sci. Lett. 163, 361–379. https://doi.org/10.1016/S0012-821X(98)00142-3.

Schwartz, S., Guillot, S., Reynard, B., Lafay, R., Debret, B., Nicollet, C., Lanari, P., Auzende, A.L., 2013. Pressure–temperature estimates of the lizardite/antigorite transition in high pressure serpentinites. Lithos 178, 197–210. https://doi.org/10.1016/j.lithos.2012.11.023.

Schwarzenbach, E.M., Caddick, M.J., Beard, J.S., Bodnar, R.J., 2016. Serpentinization, element transfer, and the progressive development of zoning in veins: evidence from a partially serpentinized harzburgite. Contrib. Mineral. Petrol. 171, 5. https://doi.org/10.1007/s00410-015-1219-3.

Shao, T., Song, M., Ma, X., Ding, X., Liu, S., Zhou, Y., Wu, J., Wang, X., Li, J., 2023. Potential link between antigorite dehydration and shallow intermediate-depth earthquakes in hot subduction zones. Am. Mineral. 108, 127–139. https://doi.org/10.2138/am-2022-8271.

Spandler, C., Pettke, T., Rubatto, D., 2011. Internal and external fluid sources for eclogite-facies veins in the monviso meta-ophiolite, western Alps: implications for fluid flow in subduction zones. J. Petrol. 52, 1207–1236. https://doi.org/10.1093/petrology/egr025.

Syracuse, E.M., van Keken, P.E., Abers, G.A., 2010. The global range of subduction zone thermal models. Phys. Earth Planet. Inter. 183, 73–90. https://doi.org/10.1016/j.pepi.2010.02.004.

Taetz, S., John, T., Bröcker, M., Spandler, C., Stracke, A., 2018. Fast intraslab fluid-flow events linked to pulses of high pore fluid pressure at the subducted plate interface. Earth Planet. Sci. Lett. 482, 33–43. https://doi.org/10.1016/j.epsl.2017.10.044.

Tian, M., Ague, J.J., Chu, X., Baxter, E.F., Dragovic, N., Chamberlain, C.P., Rumble, D., 2018. The potential for metamorphic thermal pulses to develop during compaction-driven fluid flow. Geochem. Geophys. Geosyst. 19, 232–256. https://doi.org/10.1002/2017GC007269.

Tremblay, A., Meshi, A., Deschamps, T., Goulet, F., Goulet, N., 2015. The Vardar zone as a suture for the Mirdita ophiolites, Albania: constraints from the structural analysis of the Korabi-Pelagonia zone. Tectonics 34, 352–375. https://doi.org/10.1002/2014TC003807.

Trommsdorff, V., Evans, B.W., 1972. Progressive metamorphism of antigorite schist in the Bergell tonalite aureole (Italy). Am. J. Sci. 272, 423–437. https://doi.org/10.2475/ajs.272.5.423.

Ulmer, P., Trommsdorff, V., 1995. Serpentine stability to mantle depths and subduction-related magmatism. Science 268, 858–861. https://doi.org/10.1126/science.268.5212.858.

Ulrich, M., Rubatto, D., Hermann, J., Markmann, T.A., Bouvier, A.S., Deloule, E., 2024. Olivine formation processes and fluid pathways in subducted serpentinites revealed by in-situ oxygen isotope analysis (Zermatt-Saas, Switzerland). Chem. Geol. 649, 121978. https://doi.org/10.1016/j.chemgeo.2024.121978.

van Keken, P.E., Hacker, B.R., Syracuse, E.M., Abers, G.A., 2011. Subduction factory: 4. Depth-dependent flux of H2O from subducting slabs worldwide. J. Geophys. Res., Solid Earth 116. https://doi.org/10.1029/2010JB007922.

Vrijmoed, J.C., Podladchikov, Y.Y., 2022. Thermolab: a thermodynamics laboratory for nonlinear transport processes in open systems. Geochem. Geophys. Geosyst. 23, e2021GC010303. https://doi.org/10.1029/2021GC010303.

Wilson, C.R., Spiegelman, M., van Keken, P.E., 2017. Terra FERMA: the transparent finite element rapid model assembler for multiphysics problems in Earth sciences. Geochem. Geophys. Geosyst. 18, 769–810. https://doi.org/10.1002/2016GC006702.

Yarushina, V.M., Podladchikov, Y.Y., 2015. (De)compaction of porous viscoelastoplastic media: model formulation. J. Geophys. Res., Solid Earth 120, 4146–4170. https://doi.org/10.1002/2014JB011258.

Yarushina, V.M., Wang, L.H., Connolly, D., Kocsis, G., Fæstø, I., Polteau, S., Lakhlifi, A., 2022. Focused fluid-flow structures potentially caused by solitary porosity waves. Geology 50, 179–183. https://doi.org/10.1130/G49295.1.

Yokoyama, T., Nakamura, E., Kobayashi, K., Kuritani, T., 2002. Timing and trigger of arc volcanism controlled by fluid flushing from subducting slab. Proc. Jpn. Acad. Ser. B 78, 190–195. https://doi.org/10.2183/pjab.78.190.

Yoshida, K., Oyanagi, R., Kimura, M., Plümper, O., Fukuyama, M., Okamoto, A., 2023. Geological records of transient fluid drainage into the shallow mantle wedge. Sci. Adv. 9, eade6674. https://doi.org/10.1126/sciadv.ade6674.

Zack, T., John, T., 2007. An evaluation of reactive fluid flow and trace element mobility in subducting slabs. Chem. Geol. 239, 199–216. https://doi.org/10.1016/j.chemgeo.2006.10.020.

Zhang, X., Ma, F., Yin, S., Wallace, C.D., Soltanian, M.R., Dai, Z., Ritzi, R.W., Ma, Z., Zhan, C., Lü, X., 2021. Application of upscaling methods for fluid flow and mass transport in multi-scale heterogeneous media: a critical review. Appl. Energy 303, 117603. https://doi.org/10.1016/j.apenergy.2021.117603.